REPORT DOCUMENTATION PAGE

Form Approved
OMB No. 0704-0188

Public reporting burden for this collection of information is estimated to average 1 hour per response, including the time for reviewing instructions, searching existing data sources, gathering and maintaining the data needed, and completing and reviewing this collection of information. Send comments regarding this burden estimate or any other aspect of this collection of information, including suggestions for reducing this burden to Department of Defense, Washington Headquarters Services, Directorate for Information Operations and Reports (0704-0188), 1215 Jefferson Davis Highway, Suite 1204, Arlington, VA 22202-4302. Respondents should be aware that notwithstanding any other provision of law, no person shall be subject to any penalty for failing to comply with a collection of information if it does not display a currently valid OMB control number. **PLEASE DO NOT RETURN YOUR FORM TO THE ABOVE ADDRESS.**

1. REPORT DATE (DD-MM-YYYY)
30-3-2005

REPRINT

4. TITLE AND SUBTITLE
CRRES Electric Field Power Spectra and Radial Diffusion Coefficients

5a. CONTRACT NUMBER

5b. GRANT NUMBER

5c. PROGRAM ELEMENT NUMBER

6. AUTHOR(S)
D.H. Brautigam, G.P. Ginet, J.M. Albert, J.R. Wygant*,
D.E. Rowland*, A. Ling** and J. Bass**

5d. PROJECT NUMBER
5021

5e. TASK NUMBER
RS

5f. WORK UNIT NUMBER
A1

7. PERFORMING ORGANIZATION NAME(S) AND ADDRESS(ES)
Air Force Research Laboratory/VSBXR
29 Randolph Road
Hanscom AFB MA 01731-3010

8. PERFORMING ORGANIZATION REPORT NUMBER

AFRL-VS-HA-TR-2005-1035

9. SPONSORING / MONITORING AGENCY NAME(S) AND ADDRESS(ES)

10. SPONSOR/MONITOR'S ACRONYM(S)
AFRL/VSBXR

11. SPONSOR/MONITOR'S REPORT NUMBER(S)

12. DISTRIBUTION / AVAILABILITY STATEMENT
Approved for Public Release; Distribution Unlimited.

*Univ of Minnesota, Minneapolis, Minnesota, **Radex, Inc., Bedford, MA

13. SUPPLEMENTARY NOTES

14. ABSTRACT

[1] Combined Release and Radiation Effects Satellite (CRRES) Electric Field Instrument (EFI) data are used to determine the electric field power spectral density as a function of L and Kp over the frequency range 0.2 to 15.9 mHz. The power at each frequency is fit to the function $P(L, Kp) = a \, L^b \exp(cKp)$. Assuming a purely electrostatic field and making several other assumptions regarding the azimuthal dependence of the field fluctuations, a Kp-dependent radial diffusion coefficient D_{LL}^E is computed from the power spectra. The model average D_{LL}^E for high activity (Kp = 6) are between 1 to 2 orders of magnitude larger than that for low activity (Kp = 1), dependent upon L and first invariant.

15. SUBJECT TERMS
Electron radiation belt   Diffusion coefficients   Magnetospheric   Space weather

16. SECURITY CLASSIFICATION OF:

a. REPORT	b. ABSTRACT	c. THIS PAGE	17. LIMITATION OF ABSTRACT	18. NUMBER OF PAGES	19a. NAME OF RESPONSIBLE PERSON
UNCLAS	UNCLAS	UNCLAS	SAR		Donald H. Brautigam

19b. TELEPHONE NUMBER (include area code)
781-377-3890

Standard Form 298 (Rev. 8-98)
Prescribed by ANSI Std. 239.18

CRRES electric field power spectra and radial diffusion coefficients

D. H. Brautigam, G. P. Ginet, and J. M. Albert

Air Force Research Laboratory, Space Vehicles Directorate, Hanscom Air Force Base, Massachusetts, USA

J. R. Wygant and D. E. Rowland

School of Physics and Astronomy, University of Minnesota, Minneapolis, Minnesota, USA

A. Ling and J. Bass

Radex, Inc., Bedford, Massachusetts, USA

[1] Combined Release and Radiation Effects Satellite (CRRES) Electric Field Instrument (EFI) data are used to determine the electric field power spectral density as a function of L and Kp over the frequency range 0.2 to 15.9 mHz. The power at each frequency is fit to the function $P(L, Kp) = a\ L^b \exp(cKp)$. Assuming a purely electrostatic field and making several other assumptions regarding the azimuthal dependence of the field fluctuations, a Kp-dependent radial diffusion coefficient D_{LL}^E is computed from the power spectra. The model average D_{LL}^E for high activity (Kp = 6) are between 1 to 2 orders of magnitude larger than that for low activity (Kp = 1), dependent upon L and first invariant.

1. Introduction

[2] Delineating the specific acceleration mechanisms that populate and maintain the relativistic electron radiation belt is of key interest to the magnetospheric and space weather community. There has been much attention given to various acceleration mechanisms in which the electrons interact over a range of time scales with either MHD pulses, ULF waves, or VLF waves (for a review, see *Friedel et al.* [2002]). Radial diffusion as formulated in the early 1960s [e.g., *Fälthammar*, 1965] has long been considered a fundamental acceleration mechanism that gradually (over several months time scale) energizes the radiation belt particle population. Through random perturbations, a particle's third adiabatic invariant (related to its azimuthal drift) may be violated while its first two invariants (related to its gyro and bounce motions, respectively) are conserved. Through such a stochastic process, electrons gain energy as they diffuse towards lower phase space density at lower L and greater magnetic field. A dynamic balance of radial diffusion (source) and pitch angle diffusion (loss) leads to the observed double peaked radiation belt radial profile [*Lyons and Thorne*, 1973]. More recent efforts have extended the early theoretical work on radial diffusion to include drift-resonant interactions between electrons and ULF toroidal [*Elkington et al.*, 1999] and poloidal [*Elkington et al.*, 2003] wave modes. These studies have found that these drift-resonant interactions can lead to

diffusion rates at least as significant as those predicted by the earlier treatments.

[3] Estimates of the radial diffusion coefficient due to electric and magnetic fluctuations ($D_{LL} \doteq D_{LL}^E + D_{LL}^M$) have been made from particle observations over long time intervals (months) [*Frank*, 1965; *Newkirk and Walt*, 1968; *Lanzerotti et al.*, 1970; *Lyons and Williams*, 1975; *West et al.*, 1981; *Selesnick et al.*, 1997]. These studies presume a single D_{LL} fixed for all times independent of magnetic activity. Other studies determine D_{LL}^E and D_{LL}^M from direct field measurements. *Holzworth and Mozer* [1979] analyzed electric field data from a balloon campaign at L = 6 and found a Kp-dependent D_{LL}^E. *Mozer* [1971] had earlier found that the power spectra related to D_{LL}^E show a Kp dependence but no L or local time dependence. Magnetic field power spectral densities and the corresponding D_{LL}^M have been determined at L = 4 [*Lanzerotti and Robbins*, 1973; *Lanzerotti and Morgan*, 1973] and at geosynchronous orbit [*Arthur et al.*, 1978; *Lanzerotti et al.*, 1978].

[4] It has been shown that an activity dependent D_{LL} spanning orders of magnitude is necessary (but not sufficient) to model magnetic storm time behavior of relativistic electrons [*Brautigam and Albert*, 2000]. However, until now, there has been no direct evaluation of electric field power spectral densities throughout the equatorial inner magnetosphere (L = 3.0–7.0) for a wide range of magnetic activity (Kp = 0 to 7) that could be used to directly determine $D_{LL}^E(L, Kp)$.

[5] The Combined Release and Radiation Effects Satellite (CRRES) electric field instrument (EFI) [*Wygant et al.*, 1992] has provided the opportunity to greatly extend our understanding of the inner magnetospheric electric field.

20050412 005

Previous work using CRRES EFI data has addressed the large scale DC electric field [*Rowland and Wygant*, 1998; *Wygant et al.*, 1998]. In this current study, the CRRES EFI data are used to determine the electric power spectral density as a function of L and Kp. These spectra, together with various assumptions regarding the global structure of fluctuations, are used to estimate the radial diffusion coefficient D_{LL}^E. In section 2, the CRRES orbit and electric and magnetic field instrumentation are briefly reviewed. Section 3 describes the formalism for determining D_{LL}^E in general, and outlines the approach followed here necessitated by single point measurements. The determination of the power spectral densities and the resulting D_{LL}^E are provided in section 4. Section 5 discusses the results, and concluding statements are made in section 6.

2. CRRES Orbit and Instrument Description

[6] CRRES was launched on July 25, 1990, into a geosynchronous transfer orbit (GTO) with a perigee of 350 km, an apogee of 36000 km, and an inclination of 18°. With an orbital period of 10 hours, it made a near-equatorial radial pass through the radiation belts about four times per day. The CRRES orbit's initial apogee at ~0600LT precessed through local midnight to ~1000LT in the 14 months of operation. After the initial spin-up period following launch, the satellite spin period stabilized at approximately 2 rpm with the spacecraft spin axis aligned to within 15° of the Earth-Sun line.

[7] CRRES carried instrumentation to measure both electric and magnetic fields. The electric field instrument (EFI) [*Wygant et al.*, 1992] measured the electric potential between a pair of spherical sensors and between a pair of cylindrical antennas, each orthogonal to the CRRES spin axis. The EFI signal was sampled at a rate of 32 samples/s and filtered at 10 Hz, providing a measurement of the two-dimensional electric field (in the spacecraft spin plane) with a sensitivity of better than 0.1 mV/m and a dynamic range of 1000 mV/m. The full resolution data was spin-fit to remove the sinusoidal variation of the electric field measurement resulting from the spacecraft spin. This procedure yielded the electric field components E_y and E_z in a modified GSE coordinate system (defined in section 4.1).

[8] The fluxgate magnetometer [*Singer et al.*, 1992] was comprised of three orthogonal sensors located at the end of a 6.1 m boom, and yielded 2-s resolution of the full magnetic field vector. The magnetometer operated in low (high) gain mode with a dynamic range of ±45000 nT (±850 nT) for CRRES below (above) L ~ 3.5 R_E. The magnetic field vector data permitted the estimation of the component of the electric field vector out of the spin plane from the assumption E∥ = 0.

3. Radial Diffusion Coefficient Formalism

[9] A large number of small electrostatic or electromagnetic impulses randomly perturbing an azimuthally drifting particle will lead to a net change in its radial position that can be modeled as a diffusive process. Within the radial diffusion formalism, the detailed nature of these impulses is ideally prescribed by the electrostatic (D_{LL}^E) or electromagnetic (D_{LL}^M) diffusion coefficients. In practice, a number of

simplifying assumptions must be made regarding the spatial and temporal variations of the fields involved. In this paper we are mainly interested in the contribution of electrostatic fluctuations to the radial diffusion process. For simplicity, the derivation of D_{LL}^E has traditionally assumed a symmetric dipole background magnetic field and has considered only the azimuthal component of **E** arising from convection electric field variations [*Fälthammar*, 1965; *Schulz and Lanzerotti*, 1974]. However, more recently *Elkington et al.* [2003] have investigated other forms for D_{LL} assuming a compressed dipole field and toroidal and poloidal ULF wave modes in addition to a background convection electric field. They have found that radial diffusion and energization rates increase with increasing radial distortion of the magnetic field and increasing convection electric field. These rates can be at least as significant as those for the traditional symmetric mode of diffusion, and should be considered when evaluating diffusion rates during periods when the magnetosphere experiences significant radial distortion from the impact of solar wind shocks or the interaction with high speed solar wind streams. In this study, we follow the approach outlined by [*Fälthammar*, 1965] based upon linearized theory which describes the net effect of randomly varying electric potential fields in a symmetric (dipole) field, which violate the third invariant while conserving the first and second invariants.

3.1. Electromagnetic Versus Electrostatic Fluctuations

[10] *Fälthammar* [1965] begins the derivation of the radial diffusion coefficient with the first-order equation for the time-dependent radial position (r):

$$\frac{dr}{dt} = \left(-\frac{E_\phi(r_o,\phi,t)}{B_o} + \frac{\Omega_o r_o}{3B_o} \frac{\partial b(r_o,\phi,t)}{\partial \phi} \right)_{\phi=\Omega_o t+\alpha} \quad (1)$$

where E_ϕ is the azimuthal component of the electric field, B_o is the zero-order magnetic field at radial position r_o, Ω_o is the azimuthal drift frequency, and b is the z-component of the fluctuating magnetic field. The azimuthal component E_ϕ may be expressed by the Fourier series:

$$E_\phi(r_o,\phi,t) = \sum_{n=1}^{N} E_{\phi n}(r_o,t)\cos(n\phi + \gamma(r_o,t)) \quad (2)$$

[11] For the case of electromagnetic fluctuations, both terms in the brackets of (1) are retained; **E** has a nonzero curl, and $\nabla x E = -\frac{\partial b}{\partial t}$ is used to rewrite (1) in terms of b alone. *Fälthammar* [1965] assumes a model storm magnetic field with azimuthally symmetric and asymmetric parts, and writes the magnetic radial diffusion coefficient D_{LL}^M in terms of the power spectra of the asymmetric component of the magnetic disturbance.

[12] For the case of purely electrostatic fluctuations, the second term in the brackets of (1) is time-independent and thus averages out, leaving only the electrostatic field E_ϕ. *Fälthammar* [1965] derives an expression for D_{LL}^E in terms of the summation over the power spectra $P_{\phi n}$ of the Fourier coefficients $E_{\phi n}(r_o, t)$ in (2).

3.2. Computation of D_{LL}^E

[13] No attempt has been made here to identify and separate those components of the measured electric field

fluctuations with zero curl (electrostatic) and nonzero curl (inductive). In what follows, we pursue the computation of D_{LL}^E for electrostatic fields as prescribed by *Fälthammar* [1965] and as followed by *Holzworth and Mozer* [1979].

[14] *Holzworth and Mozer* [1979] rewrote *Fälthammar*'s [1965] series expansion for E_ϕ (2) as:

$$E_\phi(L, \phi, t) = \sum_{n=1}^{\infty} E_{\phi_n}^A(L, t) \cos n\phi + E_{\phi_n}^B(L, t) \sin n\phi \quad (3)$$

where $\phi = 2\pi f t$ is the azimuthal position of the particle drifting with frequency f. As pointed out by Holzworth and Mozer, the determination of coefficients $E_{\phi n}^{A,B}(t)$ up to the n = mth term requires that $E_\phi(L, \phi, t)$ be measured at a minimum of 2m azimuthal positions for several hours continuously. At each time t, the 2m values of $E_\phi(L, \phi, t)$ are Fourier analyzed with respect to ϕ to determine $E_{\phi n}^{A,B}(L, t)$, which are then Fourier analyzed with respect to t to determine the power spectral density $P_n^{A,B}$. The total power P is determined by summing over all contributing modes:

$$P(f, L, Kp) = \sum_{n=1}^{\infty} P_n^A(nf, L, Kp) + P_n^B(nf, L, Kp) \quad (4)$$

The radial diffusion coefficient is thus given as:

$$D_{LL}^E(f, L, Kp) = \frac{c^2}{8R_E^2 B_{eq}^2} P(f, L, Kp), \quad (5)$$

where B_{eq} is the equatorial magnetic field.

[15] Given the fact of single spacecraft measurements available here, there are a number of significant approximations made in computing D_{LL}^E. First, we begin by assuming that only the n = 1 coefficients $E_{\phi 1}^{A,B}(L, t)$ are nonzero. Thus we have

$$E_\phi(L, \phi, t) = E_\phi^A(L, t) \cos \phi + E_\phi^B(L, t) \sin \phi \quad (6)$$

where the coefficients $E_\phi^{A,B}(L, t) \equiv E_{\phi 1}^{A,B}(L, t)$ are in principle determined for each time t by Fourier analyzing (in azimuth) measurements made simultaneously at multiple (≥ 2) longitudes ϕ. Although these measurements do not exist, CRRES measurements do yield the azimuthal electric field component:

$$E_\phi = -E_x \sin \phi + E_y \cos \phi \quad (7)$$

for each position (L, ϕ) and time t along the CRRES trajectory (with $\phi = 0$ at local noon). If we equate (6) and (7) and make the assumption that the measured E_x and E_y are independent of ϕ, then we can set $E_\phi^A(L, t) = E_y$ and $E_\phi^B(L, t) = -E_x$. We make the further assumption that for a given FFT interval, the satellite remains at a fixed L (a good approximation at high L, but less so at low L). We thus determine the total power spectral density P in (5) from

$$P = P_1^A + P_1^B = P_y + P_x, \quad (8)$$

where P_x and P_y are computed from the Fourier transform of E_x and E_y, respectively.

4. Power Spectral Density

[16] In this section we discuss the details for computing the x and y components of the power spectral density (solar magnetic coordinates), P_x and P_y, of the near-equatorial electric field fluctuations (0.2–15.9 mHz) as a function of L (L = 3 to 7) and magnetic activity (Kp = 0 to 7).

4.1. Data Preparation and Coverage

[17] We begin with the 30 s spin-fit electric field vector components in the spin plane (E_y, E_z) represented in a vehicle-based nonrotating coordinate system (modified geocentric solar ecliptic, MGSE). The MGSE coordinate system is defined by an x-axis that points in the positive spin axis direction (9° from the Sun), a y-axis that intersects the ecliptic and spin planes and points toward dusk, and a z-axis that completes a right-hand rectangular coordinate system. The measured **E** components are provided in the moving spacecraft reference frame and must be transformed to a stationary reference frame by subtracting the (**v** × **B**) field, where **v** is the spacecraft velocity and **B** is the locally measured magnetic field. The assumption of **E** · **B** = 0 is used to determine E_x(MGSE) from the measured E_y(MGSE), E_z(MGSE), and **B** vector field. The vector components of **E** in the MGSE system are then transformed to the solar magnetic (SM) coordinate system defined by a z-axis coincident with the magnetic dipole axis, an x-axis perpendicular to the z-axis and in the plane containing the z-axis and the Sun-Earth line, and a y-axis that completes the right-hand rule. The spectral analysis is performed on the time series for E_x(SM) and E_y(SM).

[18] It was necessary to first identify continuous intervals that met stringent "quality control" criteria, and this dramatically reduced the volume of data available for analysis. There was an electrical short in the spherical probe system that resulted in an electric field measurement that was dependent upon the plasma density and/or spacecraft potential. Also affecting the spherical probes were single event upsets, primarily during 1990. Because of these two factors, it was decided to use only the cylindrical probes.

[19] The cylindrical probes were susceptible to technical difficulties as well. During most of 1990 the cylindrical probes were improperly biased. Additionally, during 1990 the CRRES apogee was in the postmidnight sector where spacecraft charging during energetic electron injections often degraded EFI probe measurements. This study is therefore restricted to cylindrical probe data from January through October 1991 when probe biasing was optimal. This represents an immediate reduction of the data set by approximately one third, eliminating measurements from early morning local times. The local time coverage runs from ~0300LT, through midnight, and up to 1200LT, thus precluding the prenoon sector (0600LT to 1200LT).

[20] There were three other factors independent of the EFI performance that further reduced the data set. One was the routine spacecraft maneuvers that rendered the EFI signal useless and required the elimination of the 10-hour interval

following any attitude adjustment. A second was the uncertainty of spacecraft attitude and velocity that introduced error via the transformation of the measured **E** to a frame corotating with the Earth [*Wygant et al.*, 1998]. This error maximizes at low altitude where the spacecraft speed is largest and therefore this study's radial coverage is constrained to $L \geq 2.75$. A third factor was that EFI measurements were limited to the two **E** components in the spacecraft spin plane (E_y, E_z, mGSE) and thus necessitated approximating the third component (E_x, mGSE) along the spin axis. Using the assumption $\mathbf{E} \cdot \mathbf{B} = 0$ leads to $E_x = -(B_y E_y + B_z E_z)/B_x$ which introduces potentially large uncertainties in E_x for small B_x. The requirement on B_x for reliable estimates of E_x is given by $B_x > 0.5\,(B_y^2 + B_z^2)^{1/2}$; all data points failing this criterion were rejected. This led to more data being rejected throughout ~1800LT to 2000LT, over a broad range in L, than over the ranges 1300LT to 1700LT and 2000LT to 2400LT.

[21] The total number of data points in the complete CRRES/EFI database is 1.075 million. About 32% of these were rejected because they occurred in 1990 when the biasing problem was most severe, 30% were rejected because of the criterion on B_x, 17% were rejected because they were positioned below $L = 2.75$, and 1.3% were rejected because of the large perturbations caused by spacecraft attitude adjustments. The final number of remaining points is ~0.216 million, which represents ~20% of the entire database. Unfortunately, not all of these "good" data were used because intervals with a minimum number of contiguous points were required to yield a valid power spectrum.

4.2. FFT Analysis

[22] The power spectral densities, $P_1^A = P_y$ and $P_1^B = P_x$ (as in equation (8)) are determined from the Fast Fourier Transform (FFT) of $E_\phi^A(L, t) = E_y$ and $E_\phi^B(L, t) = -E_x$, respectively, where the time series intervals consist of N ($=2^n$) data points uniformly spaced in time. As is standard practice, any DC offset is first subtracted and a window function (w_k) then applied to the time series before the FFT is evaluated [*Press et al.*, 1992]. We found that various tapered windows all gave essentially the same result, and have chosen the Welch window for the final analysis.

[23] Unfortunately, the literature on power spectra can be confusing because there is no single, universally used convention defining the relation between an FFT and its power. *Fälthammar* [1965] uses the one-sided power spectrum convention of *Rice* [1954], which we adhere to as well. One may write the power spectral density in terms of the discrete Fourier transform (including the window function) as

$$P_1^{A,B}(f) = \frac{2}{W\Delta f}\left|\sum_{k=0}^{N-1} E_{\phi n}^{A,B}(k)w_k \exp(-i2\pi f k\Delta t)\right|^2, \quad (9)$$

where W is a normalization constant, $W = N\sum_{k=0}^{N-1} w_k^2$, determined from the window function. Defining Δt as the sampling time, the discrete time $t = k\Delta t$, the duration of the FFT interval is $T = N\Delta t$, and the discrete frequency step is $\Delta f = 1/T$. It should be noted that since the $E_\phi^{A,B}$ are real,

Table 1. Drift Frequencies and Energies for Fixed L and First Invariant

L	$\mu = 100$ MeV/G	$\mu = 5000$ MeV/G	$\mu = 68000$ MeV/G
3.0	0.7 MeV, 0.55 mHz	7.3 MeV, 4.3 mHz	28.1 MeV, 15.9 mHz
6.5	0.1 MeV, 0.22 mHz	2.0 MeV, 2.9 mHz	8.5 MeV, 10.8 mHz

$P_1^{A,B}(f) = P_1^{A,B}(-f)$, and (9) is evaluated for positive f only; the factor of 2 in (9) accounts for equal amounts of power at both positive and negative f.

[24] There is a trade-off between spatial and frequency resolution that requires some consideration. The set of positive frequencies is defined by $\{1/T, 2/T, \ldots, N/(2T)\}$. The Nyquist frequency $f_N \equiv N/(2T) = 1/(2\Delta t)$ is therefore fixed at 16.95 mHz given that the average sampling time $\Delta t = 29.5$s, whereas the frequency resolution $\Delta f \equiv 1/(N\Delta t)$ depends upon the chosen interval size (N). For N = 32 (T = 944s), $\Delta f = 1.06$ mHz; for N = 64 (T = 1888s), $\Delta f = 0.53$ mHz; and for N = 128 (T = 3776s), $\Delta f = 0.265$ mHz. Of particular interest is the frequency range of electric field fluctuations that resonate with the azimuthally drifting radiation belt particles. Table 1 specifies (over a range of L, energy, and corresponding drift frequency) the radiation belt electron population with which this study's E fluctuations may resonate. These electron energies range from 0.1 MeV at L = 6.5 (0.22 mHz) corresponding to the relatively common substorm injected population, to 28.1 MeV at L = 3.0 (15.9 mHz) corresponding to extremely rare acceleration events [*Li et al.*, 1993]. The main concern here is to specify the lower energy limit where the drift frequency is limited by the power spectra frequency resolution. Although the lower frequency limit would argue for the N = 128 case, the spatial resolution would be greatly compromised. The time for CRRES to traverse a fixed width in L varies with L such that within the time interval for N = 128 (3776s), CRRES may pass from L = 2.75 to 5.25, or from L = 5.25 to 6.75. Our targeted spatial resolution is ~0.5 R_E, which is more in line with N = 32 ($\Delta f = 1.06$ mHz). We ultimately chose to rely primarily on the N = 128 case, but not until we performed the complete analysis for all 3 cases (N = 32, 64, 128) and discovered that the L dependence on the power spectral density was relatively weak which meant that the spatial resolution was not a critical factor.

[25] Besides the spatial resolution, the interval size also determines the total number of FFT time series available for the study. After imposing the EFI data "quality control" criteria discussed earlier, a total of (1190, 1006, 743) valid segments of continuous data were found for the 3 values of N of interest (32, 64, 128), with the total number of points per segment ranging from N (the minimum required) to 824. It is a standard procedure to perform FFTs on overlapping intervals. The spectral variance is minimized if the intervals are offset by N/2 [*Press et al.*, 1992], but we use intervals offset by N/4 to greatly decrease the number of "excess" data points not utilized. This yields a total of 19274 16-point spectra, 7988 32-point spectra, and 2751 64-point spectra for analysis.

[26] An average L and Kp are determined for each FFT interval, and are used to sort the power spectra accordingly. The distribution of spectra over the range of L bins

Table 2. Number of Power Spectra in L and Kp Bins[a]

L =	Kp = 0	Kp = 1	Kp = 2	Kp = 3	Kp = 4	Kp = 5	Kp = 6	Kp ≥ 7
3.0	11, 0, 0	73, 0, 0	86, 0, 0	123, 0, 0	75, 0, 0	33, 0, 0	18, 0, 0	21, 0, 0
3.5	27, 6, 0	191, 70, 1	213, 76, 2	290, 113, 0	191, 70, 0	77, 29, 0	54, 26,0	53, 22, 0
4.0	26, 11, 3	196, 84, 27	250, 115, 38	326, 139, 56	207, 98, 39	94, 30, 11	69, 33, 17	66, 26, 10
4.5	26, 14, 5	199, 88, 38	305, 132, 46	363, 160, 53	250, 114, 43	116, 51, 16	82, 35, 11	78, 34, 10
5.0	34, 10, 2	261, 110, 40	369, 160, 59	418, 182, 71	317, 131, 48	152, 62, 18	82, 35, 13	81, 32, 9
5.5	49, 18, 4	347, 143, 57	449, 187, 68	525, 233, 88	455, 191, 68	189, 74, 29	94, 37, 11	65, 23, 10
6.0	50, 19, 7	487, 209, 78	665, 297, 116	674, 289, 115	619, 268, 95	238, 103, 34	90, 40, 17	108, 42, 8
6.5	68, 30, 11	852, 364, 117	1165, 514, 205	1347, 563, 203	971, 409, 149	337, 128, 36	154, 60, 24	136, 57, 22
7.0	44, 15, 2	592, 262, 97	801, 351, 131	860, 363, 130	441, 198, 70	227, 89, 26	103, 49, 17	169, 65, 20

[a]Numbers given within Kp columns are for N = 32, 64, and 128 case, respectively. L bins are 0.5 Re wide, centered on table values. Kp = 0 bin includes values (0, 0.3); Kp = 1 bin includes values (0.6, 1.0, 1.3), and so on for higher Kp.

(0.5 R_E wide) and Kp bins (integral values) are summarized in Table 2. Intervals with an average Kp ≥ 7 have been combined into a single Kp bin. The fact that the L bins are 0.5 R_E wide does not mean that the entire FFT interval fits within that bin, but only that its midpoint does; for the case of N = 128 the FFT interval may actually span between 1.5 and 2.5 R_E. Spectra for L < 2.75 were eliminated because of the error introduced by attitude
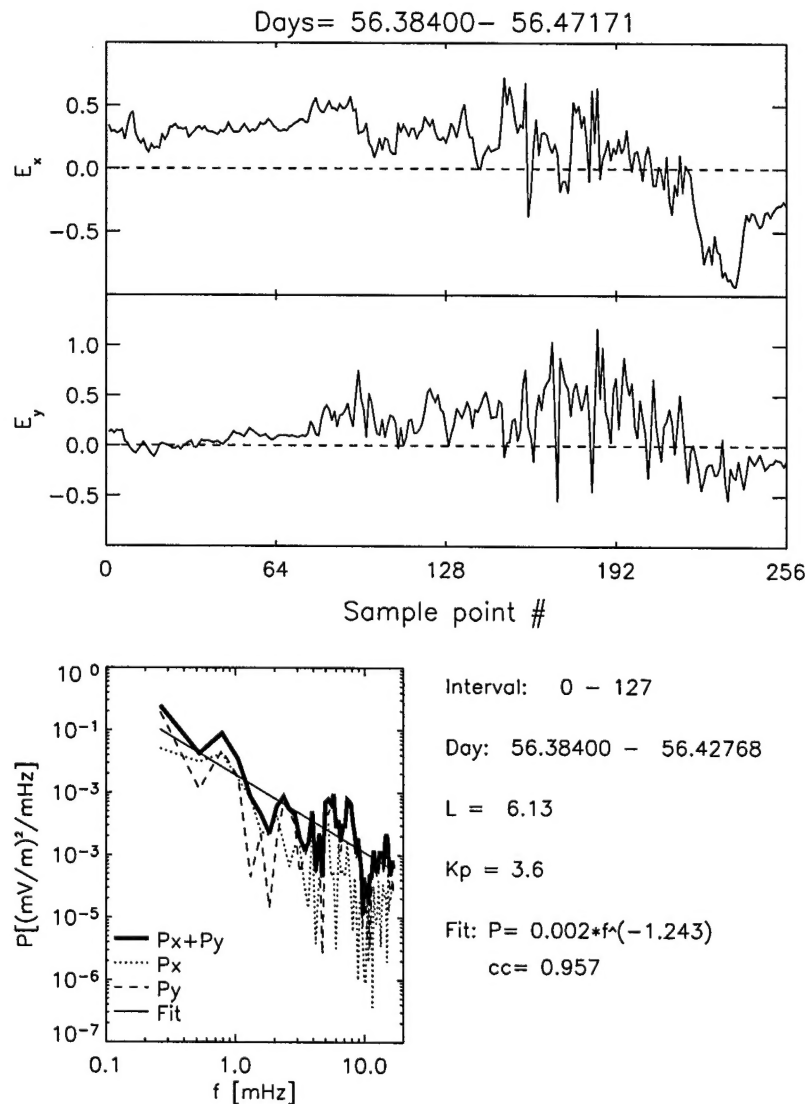

Figure 1. Top two panels show sample 256-point time series segment of E_x and E_y (mV/m) from day 56, 1991. FFTs are performed on the 128-point interval (points 0 to 127), and the resulting spectra (P_x, P_y, and $P = P_x + P_y$) are shown in the bottom panel. The endpoints (in decimal day), the average L, and the average Kp are shown for this interval. The power law fit to P is listed, with a correlation coefficient (0.957) indicating an excellent fit.
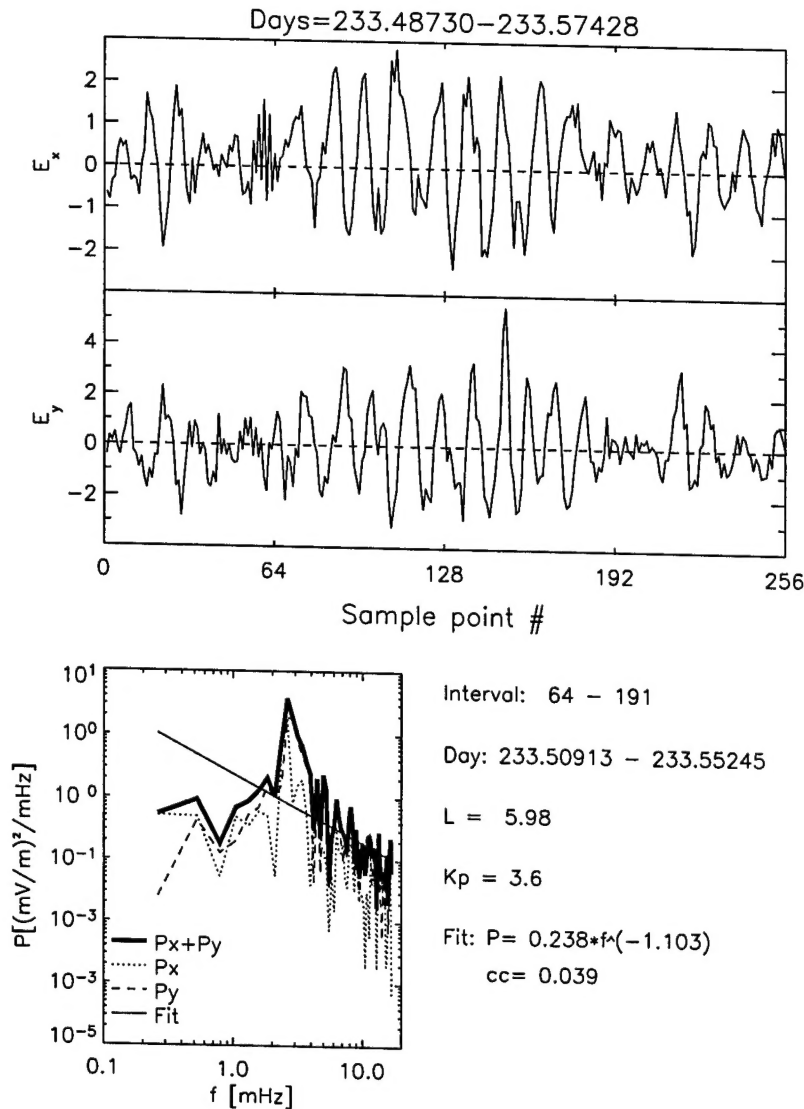
Figure 2. Same format as Figure 1, but for a segment on day 233, 1991. FFTs are performed on the 128-point interval (points 64 to 191). The power law fit to P is listed, with a correlation coefficient (0.039) indicating a poor fit due to the strong peak at 2.7 mHz.

uncertainties; those for $L > 7.25$ were eliminated because of poor statistics in that L-bin.

4.3. Power Spectral Density Model

[27] In choosing to create an empirical model of the electric field power spectral density, and hence, the radial diffusion coefficient D_{LL}^E, one must evaluate how best to parameterize the power. The temporal variability may in principle be parameterized by any number of parameters. For example, *Li et al.* [2001] have used solar wind speed (V_{sw}) fluctuations to derive a time-dependent D_{LL}, and *Mathie and Mann* [2001] have parameterized ULF power with V_{sw}. The z-component of the interplanetary magnetic field (IMF B_z) controls the magnitude of the convection electric field and may thus also be expected to determine its fluctuation power. However, throughout the CRRES mission IMP-8 was the only source of V_{sw} and IMF B_z measurements and these were too sparse for any systematic studies. The global magnetic activity index Kp has been

used in the past to parameterize electric field measurements [*Mozer*, 1971; *Rowland and Wygant*, 1998], and is used here as well. There are two alternate approaches possible to compute the model radial diffusion coefficient $D_{LL}^E(L, Kp)$. The first is to calculate the power spectra and the respective D_{LL}^E for each FFT time interval, and then sort and average the individual D_{LL}^E's according to L and Kp. The second approach is to first create an average power spectra model which can then be used to calculate the model D_{LL}^E. We follow the latter approach because the model power spectra are of interest in their own right.

[28] Figures 1 and 2 show representative E_x and E_y time series and their related power spectra. The signal in Figure 1 (day 56) has a significant DC offset, particularly obvious in the first half of the 256-point segment (sample points 0– 127) for the E_x component. The maximum peak-to-peak amplitude E_x and E_y increases from less than 0.5 mV/m during the first half of segment, to 1–1.5 mV/m during the second half. The summed power spectrum (P_x plus P_y) from
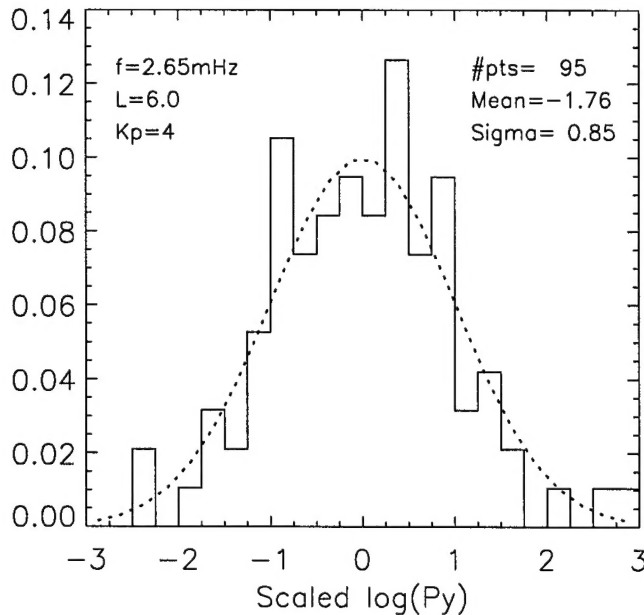
Figure 3. Histogram of the logarithmic power (P_y) at 2.65 mHz for the model bin (L = 6.0, Kp = 4). The lognormal distribution defined by a mean equal to −1.76, and standard deviation equal to 0.85 is superimposed.

the N = 128 interval (data points 0–127) is well fit by a power law in frequency with an index of −1.2 and compares well with the average power law index of −1.6 ± 0.3 found by *Mozer* [1971]. This time interval has an average L (= 6.13) and Kp (= 3.6) that assigns this spectrum to the L = 6.0, Kp = 4 model bin. The signal in Figure 2 (day 233), assigned to the same model bin but separated by 177 days, shows very different characteristics. Its maximum peak-to-peak value is 4–6 mV/m, significantly larger than the signal in Figure 1. Furthermore, there is a coherent oscillation evident in the signal that leads to a spectral peak around 2.8 mHz, thus rendering a poor fit to a power law. These coherent oscillations (with a spectral peak between 2 and 10 mHz) are common enough that the model average spectra exhibit a broad peak superimposed on an otherwise power law form. Rather than attempting to derive an analytic expression for this spectral shape, we fit the model power at each frequency as a function of (L, Kp).

[29] For each case of N (32, 64, 128), a model spectrum for $P_x(f)$ and $P_y(f)$ is computed for each (L, Kp) bin by averaging together the logarithm of the power spectra assigned to that given bin. The number of spectra in each (L, Kp) bin, for each N, is summarized in Table 2. The model power spectrum for (L = 6.0, Kp = 4) is constructed from 95 individual spectra (for N = 128); and the histogram for log P_y(f = 2.65 mHz) is shown in Figure 3. The data are well approximated by the superimposed normal distribution defined by a mean of −1.76 and standard deviation (sigma) of 0.85. The model spectrum P_y(L = 6.0, Kp = 4) for N = 128 is shown in Figure 4. The standard deviation from the average power at a given frequency is represented by vertical bars, and is seen to increase slightly with frequency. The log power at all frequencies for all model spectra is

characterized by a sigma on the order of 1, indicating that the observed power is often (~16% of the time) up to a factor of 10 times higher (or lower) than that represented by the model.

[30] As discussed in section 4.2, it is preferable to utilize the N = 128 case because its corresponding lower frequency limit provides better coverage for the ~100 keV electrons of interest to radiation belt dynamics. However, as indicated in Table 2, the N = 128 case yields essentially no spectral data in the 2 lowest L bins (L = 3.0 and 3.5). Likewise, the N = 64 case yields no data in the L = 3.0 bin. To rectify this situation, the N = 64 (32) case is used to provide spectral data for the L = 3.5 (3.0) bin, and the available spectra are extrapolated to the desired lower frequency limit (0.20 mHz). For the N = 32 case, the power at the first 3 frequencies (1.06, 2.12, and 3.18 mHz) is fit to a power law (usually a good approximation below 3.18 mHz) and extrapolated to 0.53 and 0.20 mHz. Likewise, for the N = 64 case, the power at the first 4 frequencies (0.53 to 2.12 mHz) is fit to a power law and extrapolated to 0.20 mHz. The spectra for the N = 128 case have a lower frequency of 0.26 mHz and to establish a consistent set of frequencies, the power between 0.26 and 2.12 mHz is fit to a power law and extrapolated to 0.20 mHz.

[31] To examine the validity of the extrapolation to the lowest frequencies using N = 32 spectra (at L = 3.0) and N = 64 spectra (at L = 3.5), the extrapolated values were directly compared to the N = 128 spectra case for L = 4. This comparison showed that the extrapolation to 0.2 and 0.53 mHz at L = 3.0 underestimates the spectral density by up to a factor of ~14 and ~8, respectively, and that the extrapolation to 0.2 mHz at L = 3.5 underestimates the spectral density by up to a factor of ~6.
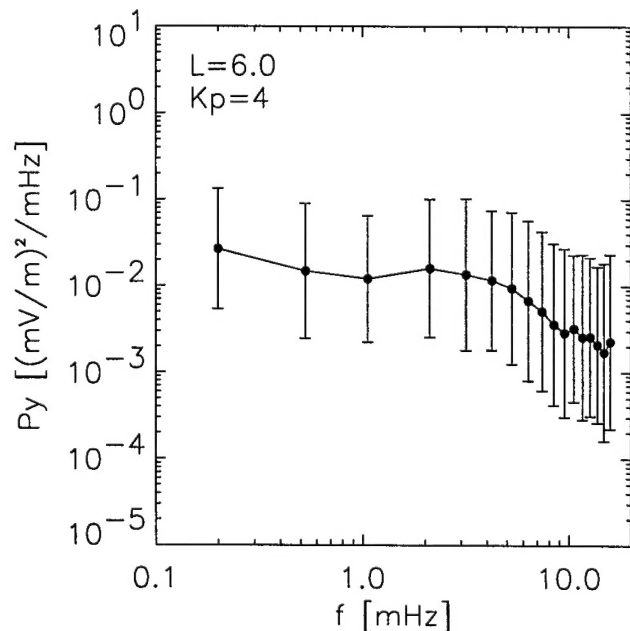

Figure 4. Model spectrum (P_y) for L = 6.0 and Kp = 4 with bars representing the standard deviation from model average.
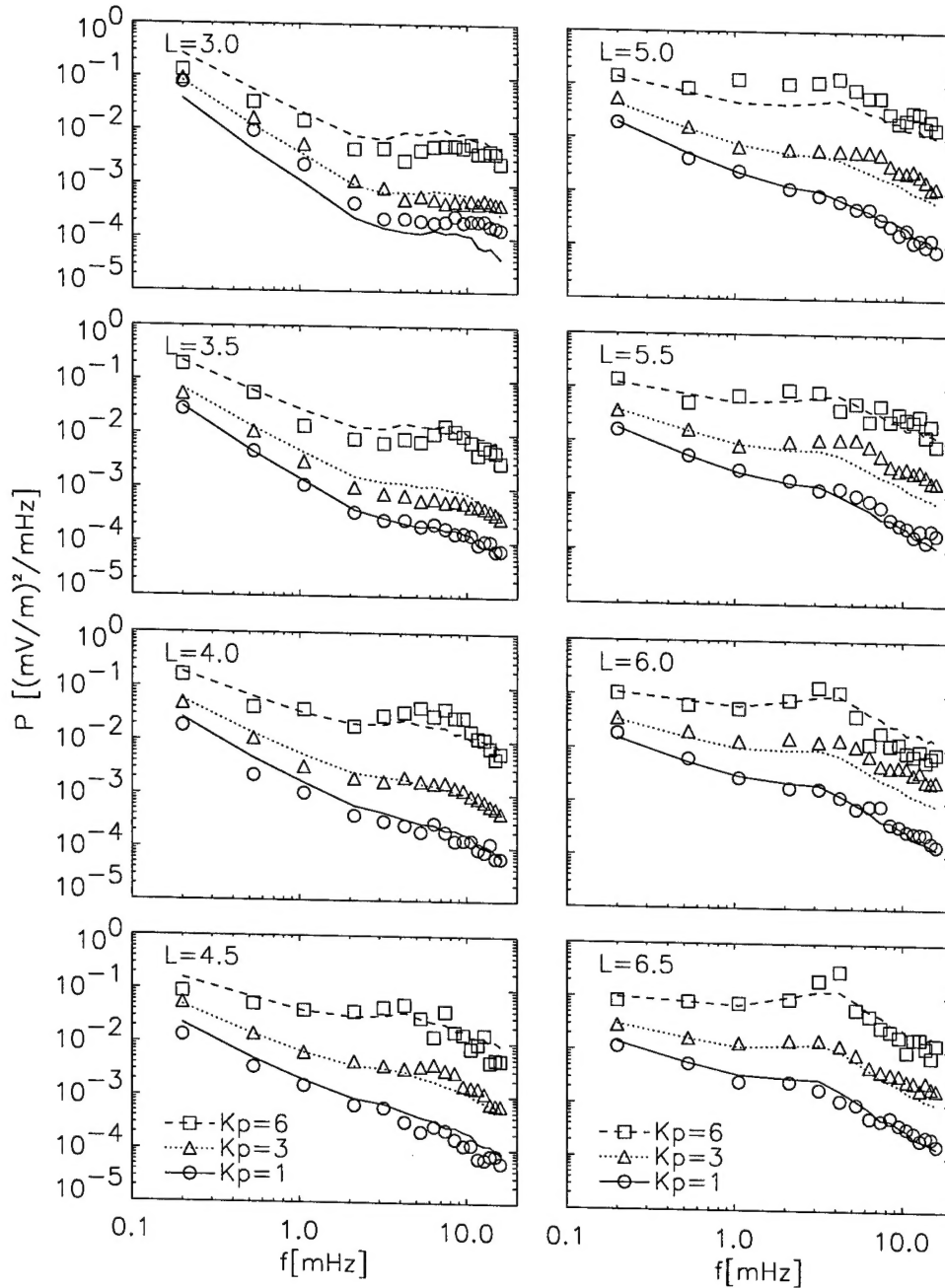
Figure 5. Model spectra $P = P_x + P_y$ for Kp = 1, 3, and 6 at L = 3.0 to 6.5 in steps of 0.5 R_E. The symbols represent the model averages; the lines represent the analytic fit to model averages, $P = aL^b\exp(cKp)$, where each frequency is independently fit as a function of L and Kp (i.e., the lines are not fits of the form power versus frequency).

[32] Considering the slow variation with frequency exhibited by the model spectra, it is felt that maintaining a resolution of 0.26 mHz for the entire frequency range is unwarranted. Furthermore, since the variance in power is much greater at the Nyquist frequency than below, we restrict the study to below the Nyquist frequency. The frequencies used in the model are chosen to be the set in common (after being extrapolated) with the three cases of N, and are as follows: 0.20, 0.53, 1.06, 2.12, ... 15.9 mHz, where a 1.06 mHz resolution is maintained above 1.06 mHz. Examples of the model total power spectra $P = P_x + P_y$ for various (L, Kp) are

illustrated in Figure 5. As noted earlier, the spectra deviate from a power law above $\sim$2–3 mHz as a result of the spectral peak from coherent oscillations in the electric field.

4.4. Power Spectral Density Fits

[33] The dependence of the total power P on (L, Kp) evident in Figure 5 is more closely examined in Figure 6 at three selected frequencies. Whereas the power at any given frequency may vary by a factor of 2 to 10 over the full range of L (3.0–7.0) for fixed Kp, it may vary by more than two orders of magnitude over the full range of Kp (0 to 7) for
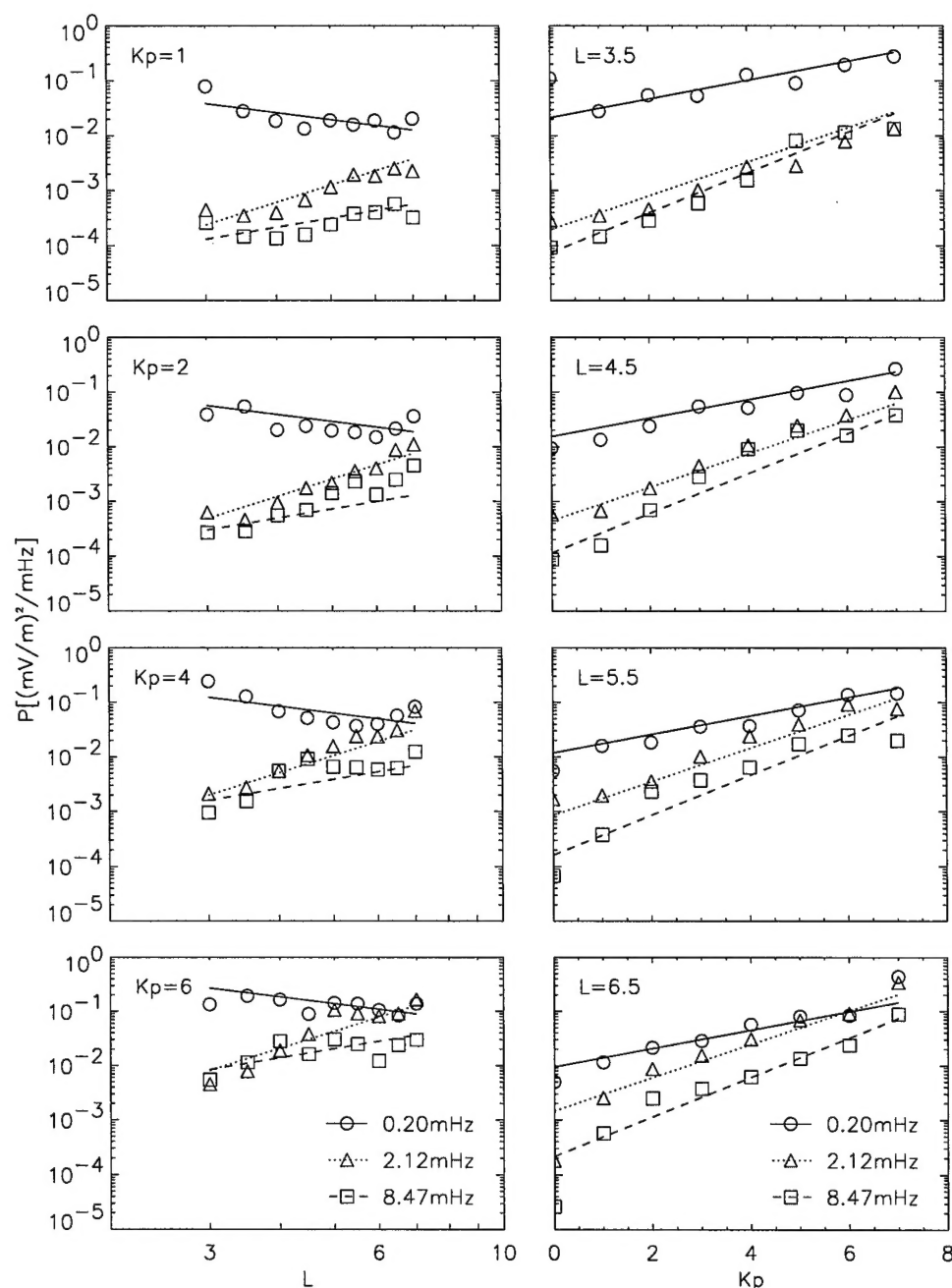
Figure 6. Plots of $P = P_x + P_y$ (at 0.2, 2.12, and 8.47 mHz) versus (left) L for (top to bottom) Kp = 1, 2, 4, and 6; and (right) P versus Kp for (top to bottom) L = 3.5, 4.5, 5.5, and 6.5. The symbols represent the model averages; the lines represent the analytic fit to model averages, $P = aL^b\exp(cKp)$, where each frequency is independently fit (as in Figure 5).

fixed L. There is least change in P at 0.2 mHz when viewed as a function of L.

[34] In fitting P as a function of (L, Kp), the range of (L, Kp) is limited to L = 3.5 to 6.5 and Kp = 1 to 6 where optimal data exist. The bins with Kp = 0 are avoided because of low statistics, and the Kp ≥ 7 bins are avoided because they represent a composite bin of Kp = 7, 8, 9. The L = 3.0 bins are avoided because of the uncertainty associated with the ($\mathbf{v} \times \mathbf{B}$) correction (greatest below L = 2.75) compounded by relatively low statistics, and L = 7.0 bins are avoided because of the uncertainty

related to off-equatorial effects. The total power at each frequency is fit to the function $P(L, Kp) = a\,L^b\exp(cKp)$ using a singular value decomposition algorithm [*Press et al.*, 1992]. We were first motivated to use the exponential dependence on Kp by *Mozer* [1971], who used $P(f, Kp) = a\exp(c\,Kp)\,f^{-n}$, and we found that this did an adequate job of fitting the data (right-hand panels of Figure 6). Unlike *Mozer* [1971], we did observe a slight dependence on L, and we found that the L^b dependence was a simple form that gave a reasonably good fit to the data (left-hand panels of Figure 6). This set of parameters {a, b, c} for

Table 3. Fit Parameters for Fixed Frequency

| Frequency, mHz | Fit Parameters of $P = a\,L^b \exp(cKp)$ | | | |
	a [$(mV/m)^2/mHz$]	b	c	Corr. Coeff.
0.20	$1.09 \cdot 10^{-1}$	−1.31	0.39	0.81
0.53	$1.56 \cdot 10^{-3}$	0.42	0.53	0.89
1.06	$1.08 \cdot 10^{-4}$	1.53	0.60	0.79
2.12	$3.24 \cdot 10^{-6}$	3.26	0.71	0.90
3.18	$1.14 \cdot 10^{-6}$	3.77	0.76	0.80
4.24	$1.35 \cdot 10^{-6}$	3.38	0.86	0.74
5.30	$2.10 \cdot 10^{-6}$	2.92	0.86	0.79
6.36	$5.21 \cdot 10^{-6}$	2.23	0.85	0.67
7.42	$6.71 \cdot 10^{-6}$	1.85	0.89	0.81
8.47	$8.45 \cdot 10^{-6}$	1.73	0.83	0.76
9.53	$8.97 \cdot 10^{-6}$	1.54	0.87	0.84
10.6	$1.06 \cdot 10^{-5}$	1.38	0.84	0.76
11.7	$5.18 \cdot 10^{-6}$	1.56	0.91	0.86
12.7	$4.39 \cdot 10^{-6}$	1.57	0.93	0.78
13.8	$6.12 \cdot 10^{-6}$	1.38	0.88	0.87
14.8	$3.91 \cdot 10^{-6}$	1.52	0.94	0.81
15.9	$2.64 \cdot 10^{-6}$	1.67	0.94	0.85

each model frequency is provided in Table 3 and is plotted in Figure 7. There is a steep gradient in the parameters (increase in b and c, decrease in a) up to 3–4 mHz, and above ~6 mHz they maintain a fairly constant value. This turning point at 3–4 mHz coincides with the point at which the model spectra in Figure 5 diverge from the power law behavior observed at lower frequencies as a result of the type of peaked spectra illustrated in Figure 2. A comparison between the model and fitted values is shown in Figures 5 and 6. In Figure 6 the comparison extends throughout the full range of L and Kp. Within the range of and L and Kp used in the fitting procedure the agreement is generally within a factor of 2.

[35] Figure 8 illustrates the degree to which this dynamic (Kp-driven) model reproduces the observed power for a given frequency (2.12 mHz) and L (6.0). To quantify the comparison we compute the following quantity as a function of the fitted model power (P^i_{fit}) and the power computed at each of the ith FFT intervals (P^i_{data}) for a given L and frequency, with the sum over the entire period of 1991 under study:

$$\delta_{model} \equiv \left(\frac{1}{npts} \sum_{i=1}^{npts} \left(\log P^i_{data} - \log P^i_{fit} \right)^2 \right)^{1/2} \quad (10)$$

For the case plotted in Figure 8, $\delta_{model} = 0.64$. Consistent with the standard deviations discussed in the preceding section, a moderate amount of discrepancy (up to a factor of ~10 too low or high) is seen between P^i_{data} and P^i_{fit}. The values of δ_{model} for all (f, L) are given in Table 4. In constructing this table's entries for L = 3.0 and L = 3.5, where 32-point and 64-point intervals are used respectively, the spectra are not extrapolated to the lower frequencies associated with the 128-point intervals; hence, the corresponding "no data" table entries. This table shows that δ_{model} increases with frequency; a trend that is consistent with the larger standard deviations observed at higher frequencies as noted in Figure 4.

4.5. Radial Diffusion Coefficients

[36] With P now determined, we can calculate the radial diffusion coefficient D^E_{LL} using equation (5). Since

the electric fields were not mapped to the equator (see section 5), the computed P are not strictly equatorial, but are up to 20° off the magnetic equator. Therefore, for consistency the D^E_{LL} is determined not with B_{eq} but with an average CRRES measured B, B_{CRRES}, determined as a function of L independent of Kp. The fitted expression for B_{CRRES} is also dipolar, with $B_{CRRES} = 4.56 \cdot 10^4 \, L^{-3}$ [nT].

[37] Radial diffusion coefficients $D^E_{LL}(f, L, Kp)$ for Kp = 1, 3, and 6 are plotted versus L in Figure 9 for first adiabatic invariants μ = 500 MeV/G (top) and μ = 5000 MeV/G (bottom). For a given μ, each value of L is associated with an equatorially mirroring particle of specified energy and corresponding drift frequency given by [Schulz and Lanzerotti, 1974]:

$$f_d = \frac{3L}{4\pi} \left(\frac{\gamma^2 - 1}{\gamma} \right) \left(\frac{c}{R_E} \right)^2 \left(\frac{m_o c}{q B_o} \right), \quad (11)$$

where γ is the relativistic factor, c is the speed of light, R_E is the Earth radius, m_o is the electron rest mass, q is
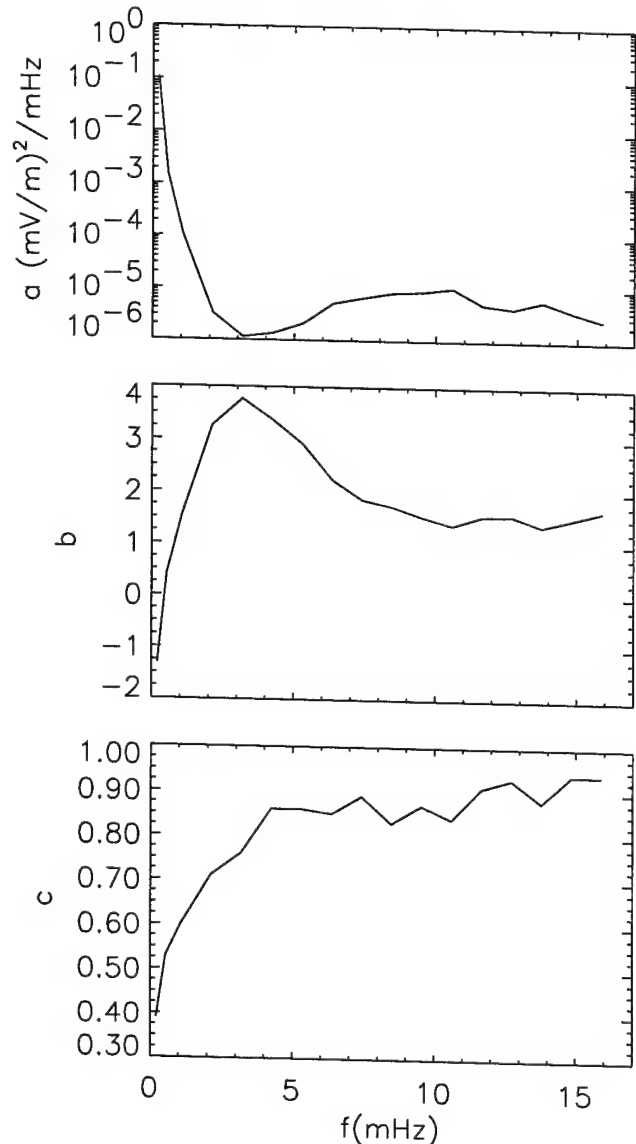

Figure 7. Fit parameters (top) a, (middle) b, and (bottom) c used in the fit $P = aL^b \exp(cKp)$, plotted versus frequency.
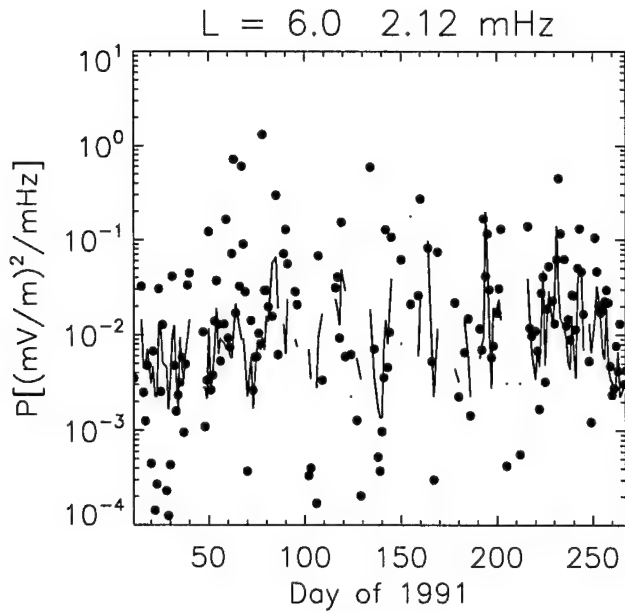
Figure 8. Comparison of observed power versus fitted model power P(f = 2.12 mHz, L = 6.0) for the full period of 1991 under study. The power observed for individual FFT intervals (P^i_{data}) is plotted as points, and the Kp-driven model power (P^i_{fit}) is plotted as a solid line. The value of Kp used to drive the model is that averaged over individual FFT intervals.

the electron charge, and B_o is the equatorial magnetic field at 1 R_E. The energies (frequencies) corresponding to 500 MeV/G range from 0.4 MeV (0.8 mHz) at L = 6.5 to 2.0 MeV (1.3 mHz) at L = 3.0. Likewise, the energies (frequencies) corresponding to 5000 MeV/G range from 2 MeV (2.9 mHz) at L = 6.5, to 7.3 MeV (4.3 mHz) at L = 3.0. It should be recalled that the values of D^E_{LL} computed for particle drift frequencies f < 1 mHz at L = 3.0 (3.5) rely on extrapolated power spectral densities from the N = 32 (64) case; otherwise, the N = 128 case is used. For the lowest frequencies, the power (and D^E_{LL})

may be underestimated by as much as an order of magnitude.

5. Discussion

[38] The procedure for mapping a purely potential convection electric field along an equipotential magnetic field line between the ionosphere (i.e., higher latitudes) and the equator has been worked out by *Mozer* [1970]. Earlier work on electric power spectra [*Mozer*, 1971; *Holzworth and Mozer*, 1979] involved balloon measurements that required implementing this mapping procedure to infer the power at the equator. Since CRRES was near the magnetic equatorial plane (between 0° and 20° magnetic latitude), and because of the uncertainties regarding the assumption of equipotential field lines, no mapping was performed for this study. Unlike the L dependence of P observed in this study, *Mozer* [1971] inferred from his ionospheric measurements that P_i (singly measured i^{th} component) at the equator was independent of L (for L = 3 to 8). He also found that by comparing power at local noon and midnight that P_i is independent of local time, something that we have not examined in this study. As noted in section 4.1, there is a significant deficit of LT coverage for various reasons. In particular, there is essentially no coverage on the dawn side from 0300LT to 1200LT, and minimal coverage on the dusk side from 1800LT to 2000LT. It has been found from space-based measurements that the predominance of ULF wave power is found in the 0600LT to 1200LT sector [*Anderson et al.*, 1990], while ground measurements suggest that during moderately active magnetic conditions (−100 nT < Dst < −50 nT) ULF wave power is at relatively low levels for the 6 hours centered on noon [*O'Brien et al.*, 2003, Plate 2]. The power and diffusion coefficients reported in this paper may be lower than those if all local times had been sampled, but it is difficult to quantify the degree to which the results may be affected.

[39] In section 4.2, the trade-off between higher spatial resolution (gained by shorter FFT intervals) versus higher frequency resolution (gained by longer FFT intervals) was discussed. In Figure 10 we plot the value of P_y(f = 2.1 mHz)

Table 4. Values of δ_{model} (Equation (10))

f, Hz	L = 3.0[a]	L = 3.5[b]	L = 4.0[c]	L = 4.5	L = 5.0	L = 5.5	L = 6.0	L = 6.5	L = 7.0
0.20	no data	no data	0.51	0.58	0.57	0.65	0.61	0.62	0.70
0.53	no data	0.51	0.58	0.61	0.57	0.60	0.56	0.59	0.75
1.06	0.64	0.54	0.55	0.52	0.56	0.60	0.58	0.58	0.67
2.12	0.60	0.59	0.56	0.60	0.62	0.67	0.64	0.64	0.70
3.18	0.59	0.57	0.57	0.59	0.63	0.71	0.72	0.68	0.70
4.24	0.61	0.62	0.61	0.69	0.76	0.72	0.68	0.73	0.81
5.30	0.62	0.68	0.75	0.71	0.71	0.79	0.81	0.73	0.81
6.36	0.67	0.65	0.72	0.74	0.74	0.84	0.80	0.75	0.84
7.42	0.68	0.72	0.75	0.79	0.81	0.82	0.88	0.80	0.82
8.47	0.67	0.67	0.75	0.71	0.82	0.83	0.85	0.84	0.91
9.53	0.74	0.75	0.72	0.74	0.84	0.90	0.84	0.86	0.89
10.6	0.75	0.77	0.76	0.76	0.89	0.94	0.85	0.87	0.92
11.7	0.77	0.82	0.80	0.84	0.86	0.85	0.87	0.85	0.93
12.7	0.84	0.77	0.76	0.80	0.86	0.91	0.91	0.83	0.94
13.8	0.86	0.81	0.81	0.78	0.85	0.88	0.86	0.83	0.93
14.8	0.89	0.78	0.82	0.75	0.87	0.88	0.88	0.88	0.95
15.9	0.88	0.79	0.84	0.82	0.89	0.94	0.87	0.85	0.98

[a]L = 3.0 statistics performed with N = 32 intervals.
[b]L = 3.5 statistics performed with N = 64 intervals.
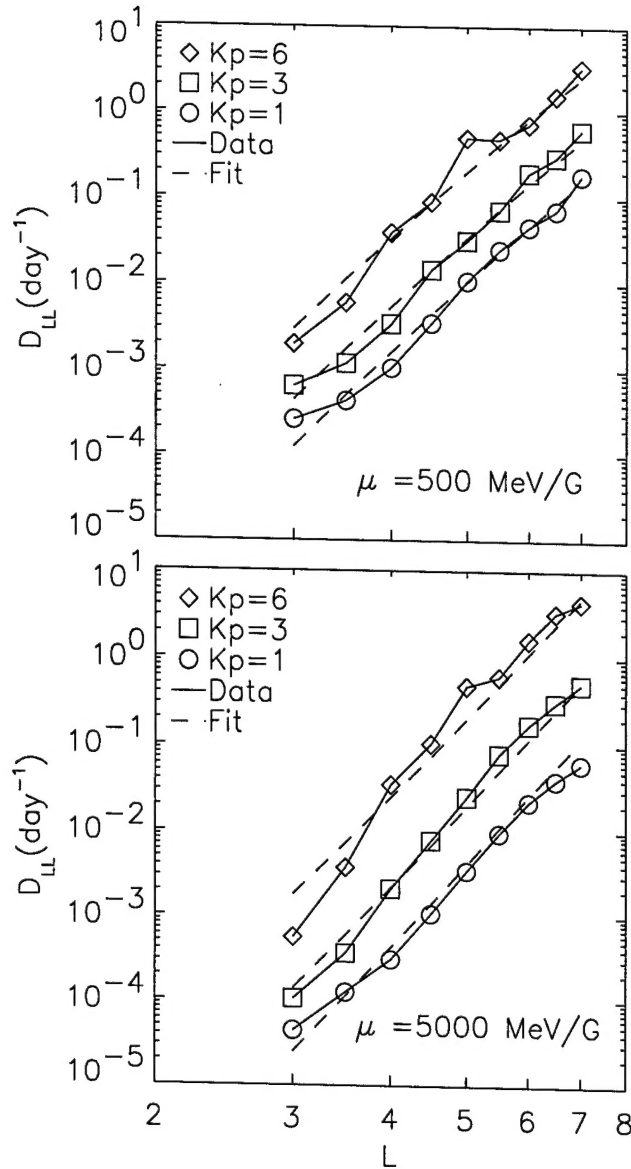[c]L ≥ 4.0 statistics performed with N = 128 intervals.

Figure 9. Plots of D_{LL}^E for fixed first adiabatic invariant (top) $\mu = 500$ MeV/G and (bottom) $\mu = 5000$ MeV/G as a function of L, for Kp = 1, 3, and 6. The symbols (keyed to Kp) with the solid lines drawn through them represent the D_{LL}^E computed with the model averages; the dashed lines represent the D_{LL}^E computed with the fitted model using the parameters in Table 3 (i.e., the dashed lines are not the "best fit" line through the symbols).

determined by a model based on N = 128 versus that for N = 32, at three different L intervals. Although the power for N = 128 is consistently greater than that for N = 32 (by less than a factor of 2), there is no significant bias in L that would affect the L dependence. Thus it appears that little was sacrificed in opting for the greater frequency resolution.

[40] *Mozer* [1971] found that the power in a single i^{th} component of electric field was given by $P_i(f, Kp) = P_o\exp(0.4Kp) \cdot f^{-n}$ with $P_o = 1.28 \cdot 10^{-2}$ (mV/m)^2/mHz, n = 1.6, and with f in mHz. As discussed in section 4.3 and illustrated in Figures 2 and 5, spectra for moderate to high

Kp exhibit peaks in the several mHz range and result in poor power law fits. These peaks are generally much less pronounced in the Kp = 1 spectra which also show little variation in L. For comparison our Kp = 1 model spectra (P_y) are averaged over all L to give $P_y = 1.52 \cdot 10^{-3}f^{-1.1}$; Mozer's result (evaluated for Kp = 1) gives $P_i = 1.91 \cdot 10^{-3}f^{-1.6}$. At 0.2 mHz, Mozer's result is ~25 times larger than our result, with this factor decreasing to ~5 at 16 mHz.

[41] The conversion of the power spectra to a radial diffusion coefficient $D_{LL}^E(f, L, Kp)$ is much more problematic than the computation of the power spectra, and is difficult to meaningfully quantify the errors involved. There are two major sources of uncertainty, and we merely raise the issues here rather than attempt to resolve them. One uncertainty arises from the complete ignorance of the azimuthal dependence of the fluctuations as discussed above. *Lanzerotti and Wolfe* [1980] point out that single point measurements of magnetic or electric field fluctuations will lead to an overestimate of radial diffusion rates because a certain fraction of power at the particle drift frequency will reside in higher frequency spatial components. There are alternatives to the azimuthal dependence assumed in this study, and it is not clear how these various models would affect the resulting D_{LL}^E. The Volland-Stern convection electric field model [*Volland*, 1978] describes a field with a component in the dawn-dusk direction only, which CRRES data clearly show is not the case. *Riley and Wolf* [1992] provide an alternative field model in terms of a finite Fourier expansion in azimuthal angle. Another model for defining the azimuthal dependence could be derived through the statistical analysis of MHD simulations. The approach followed in this study is only one way of dealing with the severe handicap of single point measurements. A second uncertainty is the determination of the relative
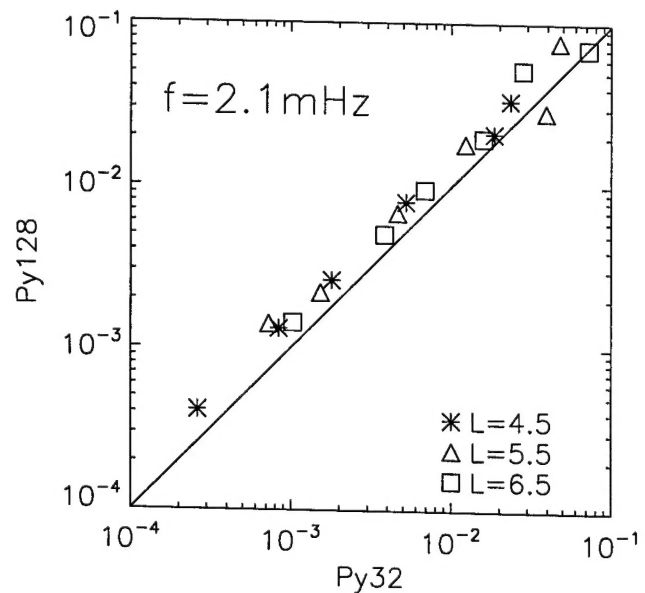

Figure 10. Plot of P_y at 2.1 mHz computed from an FFT interval with N = 128 (P_y^{128}) versus that from an interval with N = 32 (P_y^{32}). The comparison is done for three L intervals (L = 4.5, 5.5, and 6.5) as designated by the legend key. The solid line corresponds to a ratio of 1 and is included to aid the eye in comparison.

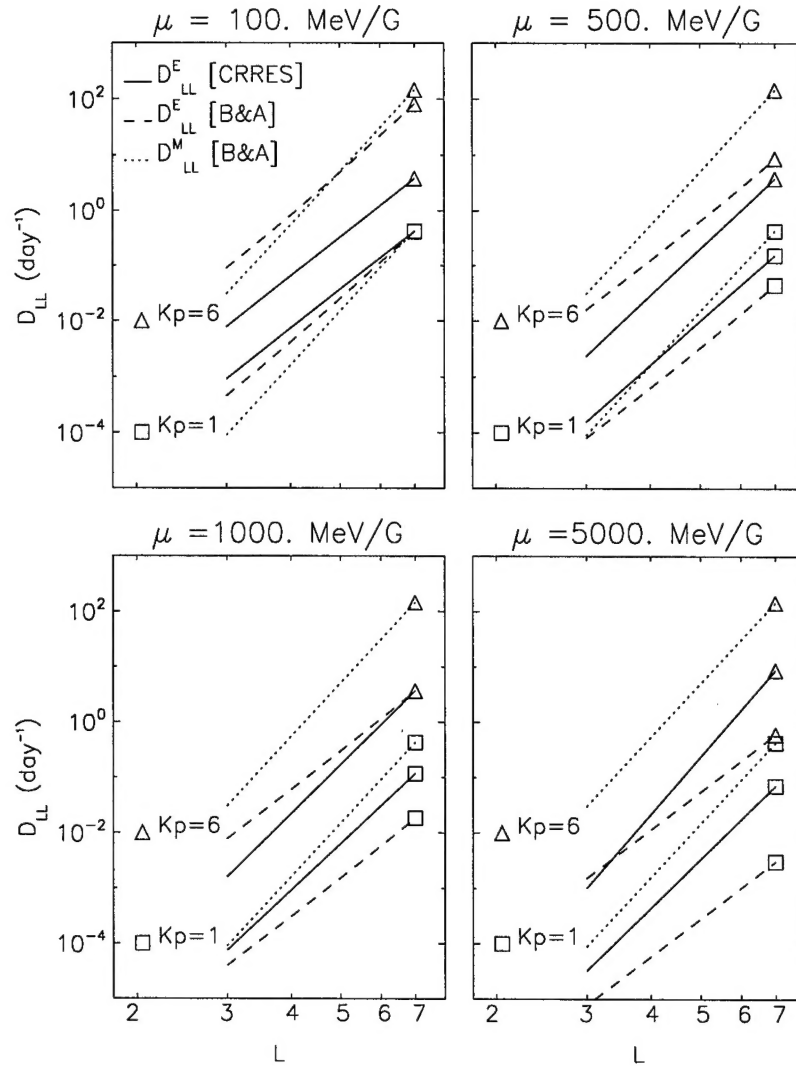**Figure 11.** D_{LL} for fixed first adiabatic invariant μ = 100, 500, 1000, and 5000 MeV/G. Plotted are the D_{LL}^E [CRRES] from this study (solid lines) as compared to the D_{LL}^E [B-A] (dashed lines) and D_{LL}^M [B-A] (dotted lines) defined by *Brautigam and Albert* [2000], for Kp = 1 (square) and Kp = 6 (triangle). The D_{LL}^E [CRRES] are drawn as best fits to the form $D_{LL}^E = D_o L^n$.

contribution from electrostatic and electromagnetic fluctuations. Progress towards quantifying these uncertainties must come from future analysis between electric and magnetic field data.

[42] Figure 11 compares this study's results D_{LL}^E [CRRES] with the Kp-dependent coefficients used previously by *Brautigam and Albert* [2000] (hereinafter referred to as B-A) to model the dynamics of an isolated magnetic storm. At μ = 100 MeV/G, for both Kp values shown, D_{LL}^E [B-A] is comparable to or exceeds D_{LL}^M [B-A]. As μ increases, D_{LL}^E [B-A] decreases and therefore its magnitude relative to D_{LL}^M (which is independent of μ) decreases. For all values of μ shown (for Kp = 1), D_{LL}^E [CRRES] exceeds D_{LL}^E [B-A]. However, D_{LL}^E [B-A] exhibits a stronger dependence on Kp so that for Kp = 6, D_{LL}^E [B-A] exceeds D_{LL}^E [CRRES] for all but μ = 5000 MeV/G.

[43] In *Brautigam and Albert* [2000] the case was made using D_{LL} [B-A] = D_{LL}^E [B-A] + D_{LL}^M [B-A] that the modeled radial diffusion could account for the μ = 100 MeV/G

dynamics reasonably well, but could not explain the dynamics (formation of peak in phase space density at L ∼ 4.5) for μ = 1000 MeV/G. As argued below, using D_{LL}^E [CRRES] in place of D_{LL}^E [B-A] is not likely to affect the general conclusions of that study. It is primarily the total D_{LL} at the higher activity levels (Kp ∼ 6) that affects the final result, so for μ = 100 MeV/G (Kp = 6), where D_{LL}^E [CRRES] ≪ D_{LL}^E [B-A] ≈ D_{LL}^M [B-A], the total D_{LL} would be ∼1/2 that of the original study, which would not affect the qualitative result for low μ. For μ = 1000 MeV/G (Kp = 6) where D_{LL}^E [CRRES] ≤ D_{LL}^E [B-A] ≪ D_{LL}^M [B-A], the total D_{LL} would be comparable to that of the original study (being dominated by D_{LL}^M) and would thus be not likely to affect the results for high μ.

[44] In addition to past estimates of D_{LL}^E and D_{LL}^M from field measurements, there have been estimates of D_{LL} from particle measurements. For example, *Selesnick et al.* [1997] have found that within the interval of L = 3 to 6, the observed dynamics of 3 to 8 MeV electrons over a 3-month

period was consistent with a $D_{LL} = 1.9 \cdot 10^{-10} \, L^{11.7 \pm 1.3}$. This compares to our result for $\mu = 5000$ MeV/G, Kp = 3, which may be fit by the form $D_{LL}^E = 9.7 \cdot 10^{-10} \, L^{10.5}$. At L = 4.5 (corresponding to an energy of 3.7 MeV) the D_{LL} from Selesnick et al. evaluates to $8.3 \cdot 10^{-3}$ day^{-1}, which is comparable to our value of $7.0 \cdot 10^{-3}$ day^{-1}.

6. Summary

[45] Using the CRRES electric field data we have modeled the power spectral density P(f) for frequencies between 0.2 and 16 mHz, as a function of L and Kp; the dependence on local time was not examined. A significant proportion of the spectra exhibit strong peaks above 2 mHz (most predominantly at ~4 mHz), thus precluding a meaningful power law fit at higher Kp as was performed by *Mozer* [1971] and *Holzworth and Mozer* [1979]. Instead, the spectral power was fit to the function $P(L, Kp) = a \, L^b \exp(cKp)$ at each frequency independently.

[46] The model spectra (in log power) are characterized by a standard deviation of ~1 (Figures 3 and 4) meaning that more than 16% of the individual power spectra differ from the model power spectra by a factor of ~10 as seen in Figure 8. This also means that the true characterization of the environment may require D_{LL}^E to be at least a factor of 10 higher or lower than the modeled D_{LL}^E despite the fact that they have been parameterized by Kp to incorporate the short-term variability.

[47] There are several significant uncertainties involved with the assumptions necessitated by single point measurements. *Lanzerotti and Wolfe* [1980] concluded their study comparing empirical estimates of D_{LL}^E and D_{LL}^M by stating that, "Substantial more work in comparing, for the same time intervals, electric and magnetic field fluctuations in space, on the ground, and at different latitudes is required in order to ultimately completely understand the temporal and spatial dependencies of the third-invariant-violating processes in the earth's magnetosphere." Nearly a quarter of a century later, we find ourselves in much the same situation. This study has taken a step forward by estimating the D_{LL}^E based on single point measurements. However, given that it is the global structure and variability of the electric and magnetic fields that control the radiation belt particle populations, it will remain near impossible to disentangle the various competing acceleration and loss mechanisms until we can better define what those fields are doing through the deployment of multisatellite constellations in coordination with ground stations.

References

Anderson, B. J., M. J. Engebretson, and S. P. Rounds (1990), A statistical study of Pc3-5 pulsations observed by the AMPTE/CCE magnetic field experiment, *J. Geophys. Res.*, *95*, 10,495–10,523.

Arthur, C. W., R. L. McPherron, L. J. Lanzerotti, and D. C. Webb (1978), Geomagnetic field fluctuations at synchronous orbit: 1. Power spectra, *J. Geophys. Res.*, *83*, 3859–3865.

Brautigam, D. H., and J. M. Albert (2000), Radial diffusion analysis of outer radiation belt electrons during October 9, 1990, magnetic storm, *J. Geophys. Res.*, *105*, 291–309.

Elkington, S. R., M. K. Hudson, and A. A. Chan (1999), Acceleration of relativistic electrons via drift-resonant interaction with toroidal-mode PC-5 ULF oscillations, *Geophys. Res. Lett.*, *26*, 3273–3276.

Elkington, S. R., M. K. Hudson, and A. A. Chan (2003), Resonant acceleration and diffusion of outer zone electrons in an asymmetric geomagnetic field, *J. Geophys. Res.*, *108*(A3), 1116, doi:10.1029/2001JA009202.

Fälthammar, C.-G. (1965), Effects of time-dependent electric fields on geomagnetically trapped radiation, *J. Geophys. Res.*, *70*, 2503–2516.

Frank, L. A. (1965), Inward radial diffusion of electrons of greater than 1.6 million electron volts in the outer radiation zone, *J. Geophys. Res.*, *70*, 3533–3539.

Friedel, R. H. W., G. D. Reeves, and T. Obara (2002), Relativistic electron dynamics in the inner magnetosphere—A review, *J. Atmos. Sol. Terr. Phys.*, *64*, 265–282.

Holzworth, R. H., and F. S. Mozer (1979), Direct evaluation of the radial diffusion coefficient near L = 6 due to electric field fluctuations, *J. Geophys. Res.*, *84*, 2559–2566.

Lanzerotti, L. J., and C. G. Morgan (1973), ULF geomagnetic power near L = 4: 2. Temporal variation of the radial diffusion coefficient for relativistic electrons, *J. Geophys. Res.*, *78*, 4600–4610.

Lanzerotti, L. J., and M. F. Robbins (1973), ULF geomagnetic power near L = 4: 1.Quiet-day power spectra at conjugate points during December solstice, *J. Geophys. Res.*, *78*, 3816–3827.

Lanzerotti, L. J., and A. Wolfe (1980), Particle diffusion in the geomagnetosphere: Comparison of estimates from measurements of magnetic and electric field fluctuations, *J. Geophys. Res.*, *85*, 2346–2348.

Lanzerotti, L. J., C. G. Maclennan, and M. Schulz (1970), Radial diffusion of outer-zone electrons: An empirical approach to third-invariant violation, *J. Geophys. Res.*, *75*, 5351–5371.

Lanzerotti, L. J., D. C. Webb, and C. W. Arthur (1978), Geomagnetic field fluctuations at synchronous orbit: 2. Radial diffusion, *J. Geophys. Res.*, *83*, 3866–3870.

Li, X., I. Roth, M. Temerin, J. R. Wygant, M. K. Hudson, and J. B. Blake (1993), Simulation of the prompt energization and transport of radiation belt particles during the March 24, 1991 SSC, *Geophys. Res. Lett.*, *20*, 2423–2426.

Li, X., M. Temerin, D. Baker, G. Reeves, and D. Larson (2001), Quantitative prediction of radiation belt electrons at geosynchronous orbit based on solar wind measurements, *Geophys. Res. Lett.*, *28*, 1887–1890.

Lyons, L. R., and R. M. Thorne (1973), Equilibrium structure of radiation belt electrons, *J. Geophys. Res.*, *78*, 2142–2149.

Lyons, L. R., and D. Williams (1975), The quiet time structure of energetic (35–560 keV) radiation belt electrons, *J. Geophys. Res.*, *80*, 943–950.

Mathie, R. A., and I. R. Mann (2001), On the solar wind control of Pc5 ULF pulsation power at midlatitudes: Implications for MeV electron acceleration in the outer radiation belt, *J. Geophys. Res.*, *106*, 29,783–29,796.

Mozer, F. S. (1970), Electric field mapping in the ionosphere at the equatorial plane, *Planet. Space Sci.*, *18*, 259–263.

Mozer, F. S. (1971), Power spectra of the magnetospheric electric field, *J. Geophys. Res.*, *76*, 3651–3667.

Newkirk, L. L., and M. Walt (1968), Radial diffusion coefficient for electrons at 1.76 < L < 5, *J. Geophys. Res.*, *73*, 7231–7236.

O'Brien, T. P., K. R. Lorentzen, I. R. Mann, N. P. Meredith, J. B. Blake, J. F. Fennell, M. D. Looper, D. K. Milling, and R. R. Anderson (2003), Energization of relativistic electrons in the presence of ULF power and MeV microbursts: Evidence for dual ULF and VLF acceleration, *J. Geophys. Res.*, *108*(A8), 1329, doi:10.1029/2002JA009784.

Press, W. H., S. A. Teukolsky, W. T. Vetterling, and B. P. Flannery (1992), *Numerical Recipes in Fortran*, Cambridge Univ. Press, New York.

Rice, S. O. (1954), Mathematical analysis of random noise, in *Selected Papers on Noise and Stochastic Processes*, edited by N. Wax, pp. 133–294, Dover, Mineola, N. Y.

Riley, P., and R. A. Wolf (1992), Comparison of diffusion and particle drift descriptions of radial transport in the Earth's inner magnetosphere, *J. Geophys. Res.*, *97*, 16,865–16,876.

Rowland, D. E., and J. R. Wygant (1998), Dependence of the large-scale, inner magnetospheric electric field on geomagnetic activity, *J. Geophys. Res.*, *103*, 14,959–14,964.

Schulz, M., and L. J. Lanzerotti (1974), *Particle Diffusion in the Radiation Belts*, Springer, New York.

Selesnick, R. S., J. B. Blake, W. A. Kolasinski, and T. A. Fritz (1997), A quiescent state of 3 to 8 MeV radiation belt electrons, *Geophys. Res. Lett.*, *24*, 1343–1346.

Singer, H. J., W. P. Sullivan, P. Anderson, F. Mozer, P. Harvey, and J. Wygant (1992), Fluxgate magnetometer instrument on CRRES, *J. Spacecr. Rockets*, *29*, 599–601.

Volland, H. (1978), A model of the magnetospheric electric convection field, *J. Geophys. Res.*, *83*, 2695–2699.

West, H. I., R. M. Buck, and G. T. Davidson (1981), The dynamics of energetic electrons in the Earth's outer radiation belt during 1968 as observed by the Lawrence Livermore National Laboratory's spectrometer on Ogo 5, *J. Geophys. Res.*, *86*, 2111–2142.

Wygant, J. R., P. R. Harvey, D. Pankow, F. S. Mozer, N. Maynard, H. Singer, M. Smiddy, W. Sullivan, and P. Anderson (1992), CRRES electric field/Langmuir probe instrument, *J. Spacecr. Rockets*, *29*, 601–604.

Wygant, J. R., D. Rowland, H. Singer, M. Temerin, F. Mozer, and M. Hudson (1998), Experimental evidence on the role of the large spatial-scale electric field in creating the ring current, *J. Geophys. Res.*, *103*, 29,527–29,544.

J. M. Albert, D. H. Brautigam, and G. P. Ginet, Air Force Research Laboratory/VSBXR, 29 Randolph Road, Hanscom AFB, MA 01731, USA. (donald.brautigam@hanscom.af.mil)

J. Bass and A. Ling, Radex, Inc., 3 Preston Court, Bedford, MA 01730, USA.

D. E. Rowland and J. R. Wygant, School of Physics and Astronomy, University of Minnesota, Minneapolis, MN 55455, USA.